

Surface Modification of CoO_x Loaded BiVO_4 Photoanodes with Ultrathin *p*-Type NiO Layers for Improved Solar Water Oxidation

Miao Zhong,^{†,‡} Takashi Hisatomi,^{†,‡} Yongbo Kuang,^{†,‡} Jiao Zhao,^{†,‡} Min Liu,^{†,‡} Akihide Iwase,[§] Qingxin Jia,^{‡,§} Hiroshi Nishiyama,^{†,‡} Tsutomu Minegishi,^{†,‡} Mamiko Nakabayashi,^{||} Naoya Shibata,^{||} Ryo Niishiro,^{‡,†} Chisato Katayama,^{‡,#} Hidetaka Shibano,[‡] Masao Katayama,^{†,‡} Akihiko Kudo,^{‡,§} Taro Yamada,^{†,‡} and Kazunari Domen^{*,†,‡}

[†]Department of Chemical System Engineering, The University of Tokyo, 7-3-1 Hongo, Bunkyo-ku, Tokyo 113-8656, Japan

[‡]Japan Technological Research Association of Artificial Photosynthetic Chemical Process (ARPChem), 5-1-5 Kashiwanoha, Kashiwa-shi, 277-8589 Chiba Japan

[§]Department of Applied Chemistry, Tokyo University of Science, 1-3 Kagurazaka, Shinjuku-ku, Tokyo 162-8601, Japan

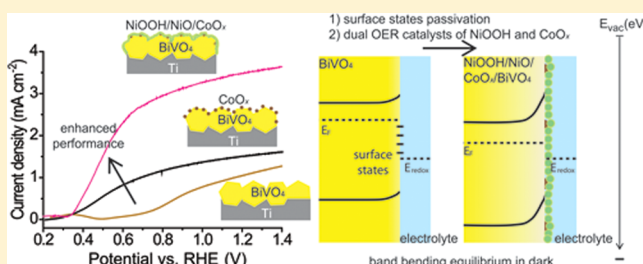
^{||}Institute of Engineering Innovation, The University of Tokyo, 2-11-16, Yayoi, Bunkyo-ku, Tokyo 113-8656, Japan

[#]Mitsui Chemicals, Inc., 580-32 Nagaura, Sodegaura, 299-0265 Chiba Japan

^{*}Fujifilm Corporation, 577, Ushijima, Kaisei-Machi, Ashigarakami-gun, 258-8577 Kanagawa Japan

Supporting Information

ABSTRACT: Photoelectrochemical (PEC) devices that use semiconductors to absorb solar light for water splitting offer a promising way toward the future scalable production of renewable hydrogen fuels. However, the charge recombination in the photoanode/electrolyte (solid/liquid) junction is a major energy loss and hampers the PEC performance from being efficient. Here, we show that this problem is addressed by the conformal deposition of an ultrathin *p*-type NiO layer on the photoanode to create a buried p/n junction as well as to reduce the charge recombination at the surface trapping states for the enlarged surface band bending. Further, the in situ formed hydroxyl-rich and hydroxyl-ion-permeable NiOOH enables the dual catalysts of CoO_x and NiOOH for the improved water oxidation activity. Compared to the CoO_x loaded BiVO_4 ($\text{CoO}_x/\text{BiVO}_4$) photoanode, the ~6 nm NiO deposited $\text{NiO}/\text{CoO}_x/\text{BiVO}_4$ photoanode triples the photocurrent density at 0.6 V_{RHE} under AM 1.5G illumination and enables a 1.5% half-cell solar-to-hydrogen efficiency. Stoichiometric oxygen and hydrogen are generated with Faraday efficiency of unity over 12 h. This strategy could be applied to other narrow band gap semiconducting photoanodes toward the low-cost solar fuel generation devices.



INTRODUCTION

In response to the rising global energy demand and the corresponding environmental concerns, producing clean and renewable fuels becomes increasingly essential.^{1–6} Among a range of possible fuel candidates, hydrogen is one of the most promising because it is carbon-neutral, high in energy density, and easily portable. It releases energy after combustion with oxygen and leaves the only byproduct of water. In this regard, extracting hydrogen from water by photoelectrochemical (PEC) devices using solar light is of particular interest, which enables recyclable use of hydrogen fuel in a green and sustainable way.^{7–13}

Constructing a high-performance PEC device generally requires highly photoactive and durable photocathodes and photoanodes for the water reduction and water oxidation reactions. Benefiting from the extensive experience gained in the electronic and solar cell industry, significant improvements have been achieved in development of the photocathodes.^{14–18}

The important *p*-type solar cell semiconductors such as silicon and III–V and I–III–VI₂ compounds are excellent light absorbers with high carrier mobility and therefore enable high solar-to-hydrogen conversion efficiencies when used as photocathodes in PEC cells. However, limited success has been achieved in photoanodes.

To expedite the PEC water splitting toward practical applications, the development of efficient and stable photoanode is crucial. The photoanodes are operated in a highly oxidizing environment, and thus the above-mentioned high-performance solar cell materials, which are extremely prone to photocorrosion, are difficult for direct use in photoanodes.

Metal oxides are superior candidates for photoanodes because they are relatively stable for water oxidation reactions.^{19–21} However, the poor charge separation in the

Received: January 9, 2015

Published: March 24, 2015

metal oxides is a major limitation, preventing their PEC performances from being optimal. To enhance the charge separation, previous researches mainly focused on (1) synthesizing high-quality nanostructures with the sizes smaller than the hole diffusion length^{22–24} and (2) increasing the electrical conductivity by donor-type dopants to reduce the resistive loss in the bulk with the applied electrical bias.^{25,26} Although these approaches have significantly improved the PEC performances, further efforts are still needed to enhance the mechanical strength of nanostructures, to realize a controllable doping profile and to reduce the external energy input of the applied bias.

In addition to the above-mentioned approaches which mainly aim to suppress the charge recombination in the bulk, another significant energy loss attributed to the charge recombination at the photoanode surface trapped states is not fully addressed. A simple and potentially efficient way to deal with this issue is to create a buried *p/n* junction at the photoanode surface. In this way, the photogenerated holes are thermodynamically extracted from the photoanode bulk and stored in the surface *p*-type material with a prolonged lifetime. The conformal deposition of an ultrathin *p*-type layer can also effectively passivate the surface trapped electrons for the reduced surface charge recombination. In addition, the deposited ultrathin *p*-type layer enables the efficient migration of the holes to the electrolyte with a small resistive loss within this layer. Among various *p*-type materials, NiO is particularly promising because it has an appropriate valence band position^{27,28} for the oxygen evolution reactions (OERs) and a strong resistance to photocorrosion in neutral and alkaline electrolytes.

Besides the efficient charge separation, a fast OER kinetics is of equal importance for high PEC performances. This requires the development of effective OER catalysts to lower the overpotential needed for the four-electron involved OERs. Solid-state catalysts such as IrO_x,²⁹ CoO_x,^{30,31} NiO,^{32,33} and NiFe₂O₄³⁴ have long been regarded as the promising electrocatalysts for dark OERs, however, only moderate activities have been achieved so far in the PEC OERs under light illumination. The amorphous “Co–Pi” discovered by Kanan and Nocera exhibits an excellent dark OER activity and durability.^{35,36} Also, the simple and low-cost fabrication process makes it amenable for mass production. However, the ultrathin “Co–Pi” layer dissolves in the pure phosphate solution at neutral pH conditions, which hinders the use of ultrathin “Co–Pi” layer for efficient PEC OERs with a minimized potential loss at this “Co–Pi” layer. To solve this problem, surface deposition of another ultrathin, nondissolving and hydroxyl-ion permeable OER catalyst layer over the “CoPi” or CoO_x is a feasible approach.

In this study, we demonstrate the efficient and stable particle-transferred photoanode made of cobalt oxide loaded BiVO₄ (CoO_x/BiVO₄) particles with Ti metal sputtered on the backside to improve electrical conductivity and an ultrathin and conformal *p*-type NiO layer deposited on the surfaces to create a buried surface *p/n* junction for the enhanced charge separation. The in situ formed hydroxyl-ion permeable NiOOH on the photoanode surface during the PEC measurements further enables the dual OER catalysts of CoO_x and NiOOH for the improved PEC performances (Figure 1).

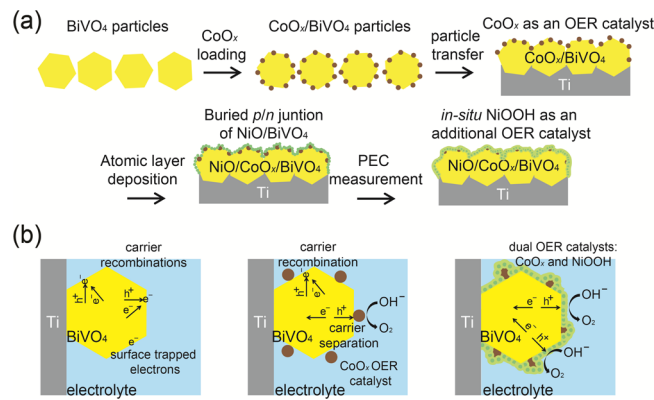


Figure 1. Fabrication of the NiOOH/NiO/CoO_x/BiVO₄/Ti photoanode and the proposed photogenerated carrier transfer process. (a) Fabrication of the NiOOH/NiO/CoO_x/BiVO₄ photoanode, including (1) synthesis of BiVO₄ particles, (2) impregnation of CoO_x on BiVO₄ with calcination, (3) sputtering of Ti metal on CoO_x/BiVO₄ particles and preparation of CoO_x/BiVO₄/Ti photoanode by the particle-transfer process, (4) atomic layer deposition of NiO on the CoO_x/BiVO₄/Ti photoanode, and (5) in situ formation of the NiOOH/NiO/CoO_x/BiVO₄/Ti structure during PEC measurement. (b) Proposed recombination/separation processes of the photogenerated carriers in the bare BiVO₄/Ti, the CoO_x/BiVO₄/Ti, and the NiOOH/NiO/CoO_x/BiVO₄/Ti photoanodes. The conformal deposition of NiO with the in situ formed NiOOH on the CoO_x/BiVO₄ surface effectively passivates the surface states, reduces the carrier recombination, and therefore enhances the PEC performances.

EXPERIMENTAL SECTION

Sample Fabrication. The NiO/CoO_x/BiVO₄ photoanode was fabricated by the following procedures: (1) synthesizing crystalline BiVO₄ particles, (2) loading CoO_x catalysts on the BiVO₄ particles, (3) drop-casting the CoO_x/BiVO₄ particles on glass substrates, sputtering Ti metals on the CoO_x/BiVO₄ particles and transferring the Ti-sputtered CoO_x/BiVO₄ particles as electrodes onto other glass substrates (the particle-transfer method),¹¹ and (4) depositing NiO on the surfaces of CoO_x/BiVO₄ electrodes by atomic layer deposition (ALD) using the Beneq TFS 200 system. The experimental details of each procedure are provided in the Supporting Information (Figure S1). The photoanode with a uniform NiO/CoO_x/BiVO₄ surface coverage can always be obtained by our controlled fabrication method. Generally, over 80% of the PEC performance is ensured.

Measurements. The scanning electron microscopy (SEM) observations were carried out using a Hitachi SU8020 system. The transmission electron microscopy (TEM), scanning transmission electron microscopy (STEM), and energy dispersive X-ray spectroscopy (EDS) analyses were conducted with ARM-200F microscopes and a JED-2300T EDS system. The X-ray photoelectron spectroscopy (XPS) analyses were performed using Mg K α (1253.6 eV) photon energy. During the XPS depth profile studies, slow Ar ion etching with an estimated etching thickness of 1–2 nm/time was used for the depth profile study. Binding energy peak shifts due to any charging were normalized with the C 1s peak set to 284.8 eV.

The PEC performances were investigated using a three-electrode electrochemical configuration in a 0.1 M KPi buffer solution at pH = 7 under simulated sunlight illumination (SAN-EI electronic, XES40S1, AM 1.5G, 100 mW cm⁻²). The electrolyte was stirred and bubbled with Ar gas before the measurements. An Ag/AgCl electrode in saturated KCl solution was used as a reference electrode and a Pt coil was used as a counter electrode. The measured potentials versus Ag/AgCl were all converted to the reversible hydrogen electrode scale according to the Nernst equation,

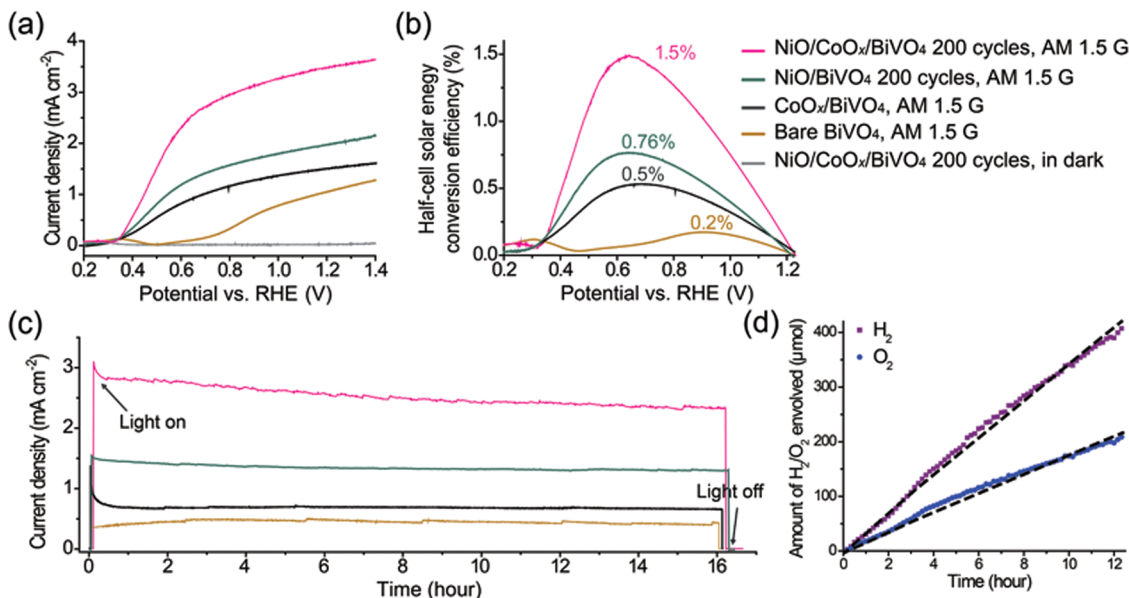


Figure 2. Solar-driven PEC performances of the BiVO₄ photoanodes in water oxidation. PEC performances of the bare BiVO₄, the CoO_x/BiVO₄ (CoO_x 1 wt %), and the NiO/CoO_x/BiVO₄ (ALD 200 cycles, CoO_x 1 wt %) photoanodes in 0.1 M KPi solution at pH 7: (a) LSV scans in dark and under AM 1.5G illumination; scan rate, 10 mV s⁻¹. (b) Half-cell solar conversion efficiencies. (c) *j*-*t* curves at 0.8 V_{RHE}; *j* is recorded at a time interval of 1 min. (d) H₂ and O₂ evolution at 1.0 V_{RHE}; dashed curves indicate the H₂ and O₂ evolution with 100% Faraday efficiency.

$$V_{\text{RHE}} = V_{\text{Ag/AgCl}} + 0.059 \text{ pH} + V_{\text{Ag/AgCl}}^{\circ}$$

$$V_{\text{Ag/AgCl}}^{\circ} = 0.199 \text{ V at } 25^\circ\text{C}$$

The potential of the working electrode was controlled via a potentiostat (Hokuto Denko, HSV-100). The scan rate is fixed at 10 mV s⁻¹ for all the PEC LSV analyses. The forward scans swept the bias from negative to positive. The solar conversion efficiency (η) is calculated from the current–potentiometry data using the following equation:

$$\eta = \frac{(J_{\text{light}} - J_{\text{dark}}) (\text{mA} \times \text{cm}^{-2}) \times (1.23 - V_{\text{RHE}}) (\text{V})}{P_{\text{sunlight}} (\text{mW} \times \text{cm}^{-2})} \times 100\%$$

where V_{RHE} is the potential of the working electrode versus the reversible hydrogen electrode in the unit of volt, J_{light} and J_{dark} are the measured photocurrent density in dark and under AM 1.5G illumination, respectively, and P_{sunlight} is the incident AM 1.5G irradiance.

An airtight three-electrode PEC cell with an Ag/AgCl reference electrode and a Pt wire counter electrode was used for gas chromatography. The PEC cell was connected to a vacuum pump and a gas chromatograph. Before the measurement, the PEC cell was pumped to low vacuum and then purged with Ar flow sufficiently until no nitrogen and oxygen gases can be detected in GC. The amount of oxygen and hydrogen evolved on the photoelectrode and the Pt counter electrode were measured with a gas chromatograph (Shimadzu, GC-8A).

RESULTS AND DISCUSSION

PEC Performance. The PEC performances of the bare BiVO₄, the CoO_x/BiVO₄ (CoO_x 1 wt %), the NiO/BiVO₄ (~6 nm NiO with ALD 200 cycles), and the NiO/CoO_x/BiVO₄ (~6 nm NiO with ALD 200 cycles, CoO_x 1 wt %) photoanodes in 0.1 M pH 7 potassium phosphate (KPi) solution are presented in Figure 2. All of the photoanodes showed low dark currents in the linear sweep voltammetry (LSV) scans, indicating that no chemical reaction occurred in dark. BiVO₄ absorbs the visible light in the solar spectrum up to 520 nm (E_g of 2.4 eV);²⁴ however, the particle-transferred bare BiVO₄

photoanode shows a low photocurrent density (j) under the simulated air mass (AM) 1.5G illumination (Figure 2a), indicating that most of the photogenerated holes are recombined before they oxidize water.

Surface loading of CoO_x (1 wt %) on the BiVO₄ can promote the charge separation³⁶ and enhance the OER activity, leading to the improved onset potential for water oxidation and also the increased PEC performance (Figure 2a). However, the obtained photocurrent density with the CoO_x/BiVO₄ photoanode is still far below the theoretical photocurrent density of the BiVO₄ calculated by converting the absorbed photons in the solar spectra. This is because the CoO_x is dispersively loaded on the BiVO₄ and it cannot fully suppress the charge recombination at the CoO_x uncovered surface areas. In addition, the CoO_x potentially dissolves in the KPi solution at neutral pH conditions, which prevents the effective use of the CoO_x surface modification for durable PEC water oxidation in moderate pH KPi electrolytes.

To cope with this issue, a *p*-type NiO layer (~6 nm) was conformally deposited on the CoO_x/BiVO₄ photoanodes by ALD to passivate the surface states as well as to create a buried *p/n* junction for the improved charge separation. The details of the NiO ALD recipes and the electrochemical characterizations are shown in the Supporting Information (Figure S2). Generally, the ALD NiO growth rate is estimated to be ~0.3 Å per cycle and the 200-cycle ALD realizes the conformal deposition of ~6 nm NiO (Figure S2). A unique advantage of the ALD is the conformal deposition^{37,38} of NiO layers with controllable thickness in the angstrom/nanometer level to wrap the BiVO₄ particles in a 3D profile (Figure S3). Importantly, the *p*-type semiconducting character of the ALD NiO is evidenced by the Mott–Schottky analysis (Figure S4), and therefore, a surface *p/n* junction effect can be anticipated.

The photocurrent density of the NiO/CoO_x/BiVO₄ photoanode reached 3.5 mA cm⁻² at 1.23 V_{RHE}, which was increased twice compared to that of the CoO_x/BiVO₄ photoanode (Figure 2a). The appearance of the anodic photocurrent at

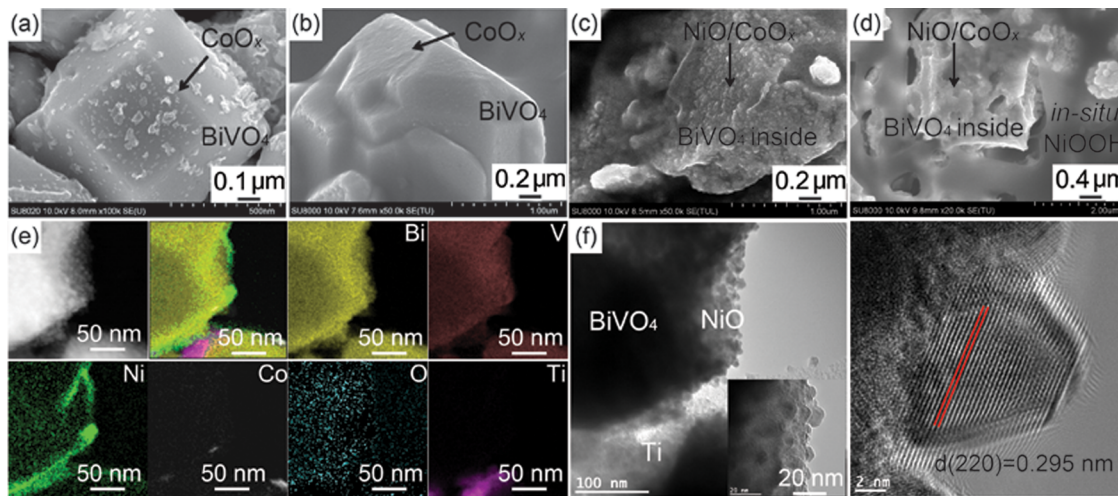


Figure 3. SEM, TEM, STEM, and EDS characterizations. (a–d) Morphologies of the $\text{CoO}_x/\text{BiVO}_4$ (CoO_x 1 wt %) photoanode before (a) and after (b) the 30 min PEC measurements in 0.1 M KPi solution at pH 7, and the $\text{NiO}/\text{CoO}_x/\text{BiVO}_4$ (\sim 6 nm NiO by 200-cycle ALD, CoO_x 1 wt %) photoanode before (c) and after the 30 min PEC measurements in 0.1 M KPi solution at pH 7 (d). (e) EDS mapping images of the $\text{NiO}/\text{CoO}_x/\text{BiVO}_4$ particle in STEM. (f) HRTEM images of the $\text{NiO}/\text{CoO}_x/\text{BiVO}_4$ particle.

\sim 0.35 V_{RHE} from the reverse LSV scan sweeping from positive bias to negative bias indicates the onset potential of the $\text{NiO}/\text{CoO}_x/\text{BiVO}_4$ photoanode, \sim 50 mV cathodically shifted relative to that of the $\text{CoO}_x/\text{BiVO}_4$ photoanode (Figure S5). A rapid increase of the photocurrent density from the onset potential, representing an improved fill factor, was obtained with the $\text{NiO}/\text{CoO}_x/\text{BiVO}_4$ photoanode. The photocurrent density reached 2.5 mA cm^{-2} at $0.6 \text{ V}_{\text{RHE}}$, a 3-fold improvement compared to the $\text{CoO}_x/\text{BiVO}_4$ photoanode. The high photocurrent density at the low potential represents a highly photoactive surface for efficient transport of holes through the photoanode surface for OERs. The half-cell solar-to-hydrogen conversion efficiency calculated from the LSV results in Figure 2a reaches 1.5% (Figure 2b), which is comparatively high among the reported single-photon photoanodes.^{24,25} The wavelength dependence of the incident photon-to-current conversion efficiency (IPCE) was examined (Figure S6). Integrating the IPCE curves using the AM 1.5G spectrum, the obtained photocurrent density agrees well with the values in the LSV curves in Figure 2a. Thus, the measured LSV data represent the steady-state PEC performance under AM 1.5G illumination.

The PEC stability of the bare BiVO_4 , the $\text{CoO}_x/\text{BiVO}_4$, the NiO/BiVO_4 , and the $\text{NiO}/\text{CoO}_x/\text{BiVO}_4$ photoanodes were compared in 0.1 M KPi at pH 7 by the chronoamperometric $j-t$ study (Figure 2c). The $\text{NiO}/\text{CoO}_x/\text{BiVO}_4$ photoanode shows a stable photocurrent density at $0.8 \text{ V}_{\text{RHE}}$ under continuous AM 1.5G illumination over 16 h with clear light on/off behaviors. Bubbles are continuously generated on the $\text{NiO}/\text{CoO}_x/\text{BiVO}_4$ surface during the stability test.

To confirm the hydrogen evolution reactions (HERs) at the Pt electrode and OERs at the $\text{NiO}/\text{CoO}_x/\text{BiVO}_4$ photoanode, the evolved gases were examined by gas chromatography (GC). The $\text{NiO}/\text{CoO}_x/\text{BiVO}_4$ photoanode was held at a constant bias of 1 V_{RHE} in a three-electrode configuration. The evolved H_2 and O_2 gases were quantified every 10 min by automatic GC integration. The total amounts of the evolved H_2 and O_2 gases were 390 and $198 \mu\text{mol}$ after 12 h (Figure 2d). No nitrogen gas was detected during the 12 h test, indicating that there is no air leaking in our GC system. Stoichiometric evolution of H_2 and

O_2 with a ratio of virtually two was obtained. The faraday efficiency for the HERs and OERs are found by counting the electrons passing through the PEC cell to be both close to 100%. These results confirm that the photocurrent was attributed to the OERs and HERs, and thus the half-cell solar-to-hydrogen conversion efficiency can be calculated using the measured LSV curves under AM 1.5G.

Characterization. SEM images of the $\text{CoO}_x/\text{BiVO}_4$ (CoO_x 1 wt %) and the $\text{NiO}/\text{CoO}_x/\text{BiVO}_4$ (\sim 6 nm NiO by 200 ALD cycles, CoO_x 1 wt %) photoanodes before and after the PEC measurements are presented in Figures 3 and S7. The CoO_x particles (\sim 10–30 nm) were dispersively loaded on the surfaces in the as-synthesized $\text{CoO}_x/\text{BiVO}_4$ photoanode (Figure 3a). After the 30 min PEC measurement in 0.1 M KPi solution at pH 7, small nanogranules were observed (Figure 3b). These nanogranules were likely the CoO_x in situ formed during the PEC measurement.³⁶ The CoO_x gradually dissolves in the KPi solution, as indicated by the decrease of the photoanodic current in LSV scans in new KPi solutions (Figure S8).

To prevent the CoO_x leaking from the surface, \sim 6 nm NiO was deposited over the $\text{CoO}_x/\text{BiVO}_4$ particles by 200-cycle ALD. As shown in Figure 3c, the NiO nanoparticles were uniformly deposited on the $\text{CoO}_x/\text{BiVO}_4$ photoanode. After the 30 min PEC measurement, thin flat and translucent films were observed on the top of NiO particles (Figure 3d). The translucent film was likely the NiOOH in situ formed during the PEC measurement.^{32,33} This is evidenced by the XPS analyses as discussed later.

To characterize the structure and the crystalline quality of the $\text{NiO}/\text{CoO}_x/\text{BiVO}_4$ particles, TEM, and EDS analyses were performed. The EDS element mapping profiles in Figure 3e reveal that NiO was homogeneously deposited on the BiVO_4 surface. TEM images of the $\text{NiO}/\text{CoO}_x/\text{BiVO}_4$ particles in different magnifications are shown in Figure 3f. The size of the NiO nanoparticles is in the range of 5–10 nm, which agrees well with the SEM results. The single crystal NiO nanoparticle with an interplanar spacing of \sim 0.295 nm corresponding to the NiO (220) plane is clearly observed.

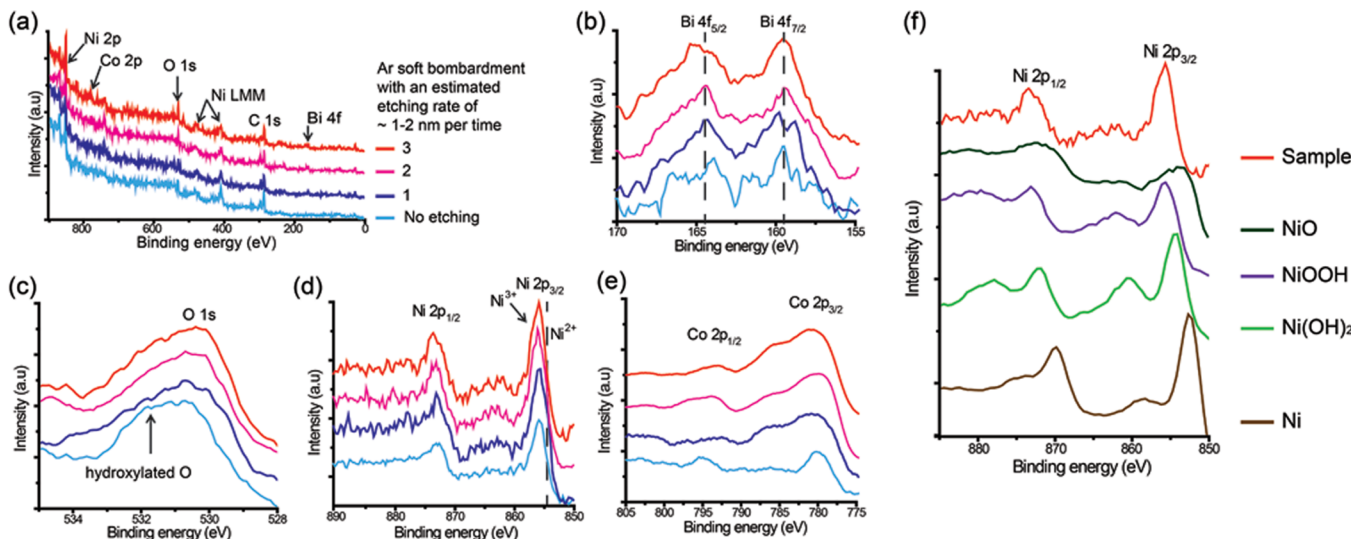


Figure 4. XPS analyses. (a–e) XPS analyses of the $\text{NiO}/\text{CoO}_x/\text{BiVO}_4$ photoanode after the PEC measurements under soft Ar bombardment: (a) XPS survey spectra, (b) high resolution XPS spectra of Bi 4f, (c) O 1s, (d) Ni 2p, and (e) Co 2p. (f) High resolution XPS Ni 2p spectra obtained with the Ni metal, the NiO, the $\text{Ni}(\text{OH})_2$, the NiOOH , and the $\text{NiO}/\text{CoO}_x/\text{BiVO}_4$ after-PEC-measurement photoanode.

To ascertain the constituent compositions and the chemical states of the $\text{NiO}/\text{CoO}_x/\text{BiVO}_4$ (200-cycle ALD, CoO_x 1 wt %) photoanode after the PEC measurement (the same sample of Figure 3d), XPS analyses were conducted. As shown in the XPS survey spectra in Figure 4a, Bi, O, Ni, and Co elements were continuously detected during the soft Ar bombardment. The binding energy peak of ~ 159 eV is determined for the Bi 4f_{7/2}, which is coincident with the reported value.²⁰ The Bi 4f_{7/2} and the Bi 4f_{5/2} peak positions remain unchanged upon Ar etching, but intensities increase with Ar etching (Figure 4b), indicating more BiVO_4 is exposed with soft Ar bombardment.

Importantly, the hydroxyl O 1s peaks was observed in Figure 4c, indicating the hydroxylated surface of the $\text{NiO}/\text{CoO}_x/\text{BiVO}_4$ photoanode. It is consistent with the SEM observation of the translucent NiOOH film on the $\text{NiO}/\text{CoO}_x/\text{BiVO}_4$ surface (Figure 4d). The peak intensity ratio between the hydroxyl O 1s and the oxide state O 1s decreases with Ar etching, indicating the surface OH ions are bombarded out during the Ar bombardment. As reported, the NiOOH is an OER catalyst for dark electrolysis.^{24,32} A smaller overpotential was needed to obtain the same current density with the $\text{NiO}/\text{CoO}_x/\text{FTO}$ electrode compared to the CoO_x/FTO electrode (Figure S9).

As shown in Figure 4d, the Ni 2p_{3/2} peaks with a predominant intensity close to a higher binding energy over 856 eV, which is more positive than the typical divalent Ni species binding energy in NiO (854–855 eV), are constantly observed in the narrow scans after Ar bombardment. This is indicative of the presence of trivalent Ni species. To further ascertain the formation of Ni^{3+} (in NiOOH) on the BiVO_4 surface, the Ni 2p_{3/2} XPS spectra of the $\text{NiO}/\text{CoO}_x/\text{BiVO}_4$ after the PEC measurement, the Ni metal, the NiO powder (Wako), the $\text{Ni}(\text{OH})_2$ powder (Aldrich), and the synthesized NiOOH were measured (Figure 4f). The details of the NiOOH synthesis are described in the Supporting Information with XRD characterizations (Figure S10). It is therefore evidenced that NiOOH was formed on the $\text{NiO}/\text{CoO}_x/\text{BiVO}_4$ photoanode surface during our PEC measurement.

The existence of the buried CoO_x in the $\text{NiO}/\text{CoO}_x/\text{BiVO}_4$ photoanode after PEC measurement is further evidenced. Co

2p_{1/2} and 2p_{3/2} peaks close to the Co^{2+} 2p binding energy positions were clearly detected in the XPS analyses (Figure 4e). Compared to the Ni signal intensity, the detected Co signal intensity is much smaller indicating that the amount of CoO_x loaded by impregnation method is much smaller compared to that of NiO by ALD. It agrees with the EDS analyses in Figure 3e. Therefore, the structure of $\text{NiOOH}/\text{NiO}/\text{CoO}_x/\text{BiVO}_4$ is inferred as shown in Figure 1.

Open-Circuit Photovoltage and Surface Band Bending Diagrams. A *p/n* junction serves an important role in the semiconductor based electronic devices. For example, high-quality *p/n* junctions are key building blocks in solar cell devices enabling efficient charge separation to achieve high energy conversion efficiencies. In the photoanode-based half-cell water splitting scheme, the efficient charge separation is also of first importance to realize high PEC performances. Further, the separated holes on the half-cell photoanode surfaces should have a long lifetime to oxidize water before they are recombined with electrons at the surface states. Thus, the enhanced OERs is always obtained when coupled with effective OER catalysts.

To study the possible *p/n* junction effect, the PEC performances of the four BiVO_4 photoanodes in Figure 2a were measured in 0.1 M KPi solution with the presence of 1 M Na_2SO_3 as a hole scavenger under AM 1.5G illumination (Figure S11). The oxidation of sulfite is thermodynamically and kinetically easier than the oxidation of water,²⁴ and therefore, it allows us to compare the charge separation abilities in different photoanodes by comparing their photocurrent density regardless the slow OER kinetics. It is observed that the photocurrent density increases from the bare BiVO_4 to the $\text{NiO}/\text{CoO}_x/\text{BiVO}_4$ photoanodes in the sulfite solution indicating the increased charge separation with the buried *p/n* junctions. Different from the photoelectrochemical deposition or electrochemical deposition of amorphous FeOOH ,²⁴ NiOOH ,²⁴ and CoPi ,^{25,35} our impregnated CoO_x and ALD NiO are both calcined at 300 °C for more than 1 h. This process helps the crystallization of CoO_x and NiO on BiVO_4 to realize the buried *p/n* junctions.

To examine the functionality of the ALD NiO layers on the $\text{CoO}_x/\text{BiVO}_4$ photoanodes, thickness dependence study was performed using 100- to 300-cycle ALD NiO and fixing CoO_x in 1 wt %. Compared to the $\text{CoO}_x/\text{BiVO}_4$ photoanode, the PEC performances of the $\text{NiO}/\text{CoO}_x/\text{BiVO}_4$ photoanodes (ALD 100–300 cycles) are improved (Figure 5a). It suggests

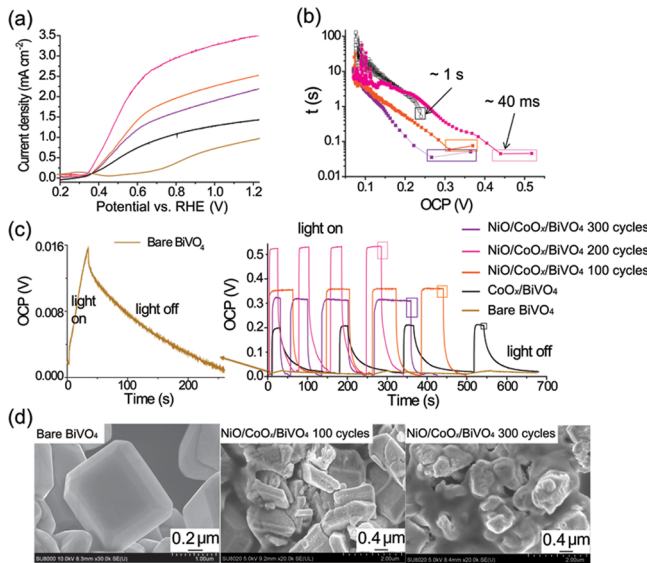


Figure 5. ALD NiO thickness dependent study. (a) LSV scans under AM 1.5G illumination of the bare BiVO_4 , the $\text{CoO}_x/\text{BiVO}_4$ (CoO_x 1 wt %) and $\text{NiO}/\text{CoO}_x/\text{BiVO}_4$ (ALD 100, 200, and 300 cycles, CoO_x 1 wt %) photoanodes in 0.1 M KPi solution at pH 7. (b) Carrier lifetime derived from OCP-decay curve at the transient when illumination is removed at the OC condition and plotted as a function of OCP in a logarithm scale. The results were measured in 0.1 M KPi solution at pH 7. (c) OCP values in 0.1 M KPi solution at pH 7 under AM 1.5G illumination and in dark. (d) SEM images of the bare BiVO_4 , the 100-cycle $\text{NiO}/\text{CoO}_x/\text{BiVO}_4$, and 300-cycle $\text{NiO}/\text{CoO}_x/\text{BiVO}_4$ photoanodes after the PEC measurement.

that the conformal deposition of NiO on BiVO_4 surfaces forms buried p/n junctions and effectively passivates the BiVO_4 surface states for the enlarged charge separation. In addition, the in situ formed NiOOH may further work as an OER catalyst to promote the OERs. Note that the NiOOH layer should be thin enough to efficiently transport holes through the NiOOH film for OERs. Otherwise, the electron–hole recombination occurs in the thick NiOOH film and decreases the PEC performance.^{32,33} In our case, the NiOOH film in the 300-ALD-cycle $\text{NiO}/\text{CoO}_x/\text{BiVO}_4$ photoanode was apparently thicker (Figures 5d and S12). This can be also evidenced by observing the interface resistances using the electrochemical impedance spectroscopy analyses. The NiOOH resistance increased to $\sim 5.5 \text{ k}\Omega$ in the 300-ALD-cycle photoanode compared to that of $\sim 1 \text{ k}\Omega$ for 200-ALD-cycle photoanode (Figure S13). Overdeposition 500-ALD-cycle NiO largely increased the NiOOH resistance to $\sim 55 \text{ k}\Omega$ and significantly decreases the PEC performance.

To further discuss the enhanced PEC performances with the CoO_x and NiO modifications, the open circuit photovoltage (OCP) of the photoanodes in the same solution of 0.1 M KPi at pH 7 in dark and under AM 1.5G illumination were measured. OCP = open circuit voltage upon AM 1.5G illumination ($\text{OCV}_{\text{light}}$) – open circuit voltage in dark (OCV_{dark} , also known as resting potential) represents the

amount of the band bending at the time being with respect to that in the dark condition, for each of the constructed electrode structures. OCV is the most positive in dark due to the largest energy band upward bending, and OCV is more cathodic under illumination, with the energy band rather flattened by photoexcited carriers.^{39–41} The degree of the band bending is determined by the built-in potential in the photoanode/electrolyte junction, the minority carrier accumulation and the charge recombination. An enlarged band bending at the photoanode/electrolyte interface represents the enhanced electron–hole separation. We demonstrate that the conformal deposition of *p*-type NiO on the $\text{CoO}_x/\text{BiVO}_4$ surface effectively enlarges the band bending. The OCP is systematically increased from the bare BiVO_4 to the $\text{CoO}_x/\text{BiVO}_4$ and to the 200-ALD-cycle $\text{NiO}/\text{CoO}_x/\text{BiVO}_4$ photoanode (Figure 5c). OCP decreases in the 300-ALD-cycle $\text{NiO}/\text{CoO}_x/\text{BiVO}_4$ photoanode, presumably because of the increased electron–hole recombination in the thick NiOOH film. The OCPs are repeatable under intermittent irradiation (Figure 5c) and consistent with the corresponding PEC performances. Note that kinetic or catalytic effect should be ruled out in the open circuit condition as current arising from the assumed redox reactions does not pass steadily. These observations indicate that the formation of an enlarged band bending at the photoanode/electrolyte junction is decisive for the high PEC performance.⁸

The schematic illustrations of the band bending corresponding to the measured absolute OCV_{dark} and $\text{OCV}_{\text{light}}$ values of the bare BiVO_4 , the $\text{CoO}_x/\text{BiVO}_4$, and the $\text{NiO}/\text{CoO}_x/\text{BiVO}_4$ photoanodes are shown in Figure S14. The more cathodic $\text{OCV}_{\text{light}}$ values indicate the flattened energy band of the photoanodes (in light quasi-equilibrium with the electrolyte) by the photoexcited carriers. $\text{OCV}_{\text{light}}$ is mostly determined by the negatively Fermi level shifts in the photoanode materials under illumination. In contrast, the OCV_{dark} reflects the upward band bending nature of the photoanodes in dark equilibrium with the electrolyte. More positive OCV_{dark} values were obtained with the $\text{NiO}/\text{CoO}_x/\text{BiVO}_4$ samples suggesting the effective passivation of the BiVO_4 surface states for the reduced surface Fermi leveling pinning effect. As a result, the enlarged band bending was formed after the conformal ALD NiO deposition. It is necessary to mention that our OCV measurements were performed under Ar bubbling conditions, which is the same condition in the PEC photocurrent measurements. In addition, the Ar bubbling rules out the possibility of the surface states passivation by the surface O_2 absorption in the O_2 saturated electrolyte. Therefore, we can conclude that the improved OCPs were realized at the photoanode/electrolyte junction by the conformal ALD NiO surface modifications.

Another way to probe the photoanode/electrolyte junction quality is to study the lifetime of the mobile photogenerated carriers as a function of OCP. At the transient from the illuminated quasi-equilibrium of the most flattened energy band to the dark equilibrium of the most bent energy band at the OC condition, the charge recombination is mainly determined by the spatial charges built in the photoanode/liquid junction. The enlarged band bending enables the increased amount of spatial charges in the depletion region and thus the charge recombination is enhanced at the transient when the illumination is stopped.³⁹ As a result, a fast OCP-decay is expected (Figure 5c). Using the equation developed by Zaban et al.,³⁹

$$\tau = -\frac{k_B T}{e} \left(\frac{dOCP}{dt} \right)^{-1}$$

where τ is the carrier lifetime, $k_B T$ is the thermal energy, and e is the positive element charge, the carrier lifetime can be quantified for comparison of the charge recombination rate in the junction.

In the NiO/CoO_x/BiVO₄ photoanodes, the carrier lifetime is ~40 ms at the transient when the illumination is stopped at the open-circuit condition in 0.1 M KPi buffer solution at pH 7 (Figure Sb). It is decreased by a factor of 25 compared to that of ~1 s for the CoO_x/BiVO₄ photoanode. This is indicative of the enhanced charge recombination when illumination is stopped. Consequently, the enhanced charge separation is expected in the same junction under illumination. Note that the fast OCP-decay behavior for the NiO/CoO_x/BiVO₄ photoanodes is obtained in the pH 7 electrolyte in which the OH⁻ concentration is relatively small compared to that in the high pH electrolyte. It suggests the in situ formed hydroxyl-rich NiOOH on the NiO/CoO_x/BiVO₄ surface improves the BiVO₄/CoO_x/NiO/NiOOH/electrolyte solid/liquid junction quality.

Note that the conformal *p*-type NiO surface passivation could prevent the surface trapped electrons to be in directly contact with the electrolyte and therefore reduce the surface charge recombination. To further study that the surface passivation effect for BiVO₄, we deposited 5 and 10 nm conformal ALD Al₂O₃ layers over the CoO_x/BiVO₄ photoanodes, because Al₂O₃ is widely used as a dielectric passivation layer for both *p*-type and *n*-type silicon to reduce the interface charge recombination in solar cell devices. It is found that the fast OCP-decay behavior is obtained with the Al₂O₃/CoO_x/BiVO₄ photoanodes, indicating that the free mobile photogenerated carriers are improved after the Al₂O₃ surface passivation⁷ (Figure S15). However, the OCP values decrease with the increased ALD cycles of Al₂O₃. This is because the dielectric Al₂O₃ does not offer *p/n* junction effect to enlarge the band bending at the photoanode surface. In addition, the OER activity of Al₂O₃ is negligible compared to that of NiO resulting in the decreased PEC performances. It is therefore suggested that the high-efficiency charge separation and the high-performance OER activity are both the rate-determine factors for PEC OER activity.

Finally, a parametric study was performed by changing the amount of CoO_x and fixing the 200-cycles ALD NiO to quantify the CoO_x and NiO amount on BiVO₄ for the best PEC performance. The SEM images of the different amount CoO_x-loaded BiVO₄ samples are shown in Figure S16. The excessive loading of CoO_x (1.5 wt %) leads to the aggregation of the CoO_x/BiVO₄ particles during the postannealing process, resulting in the decreased PEC performances. The experimental results confirm that the NiO/CoO_x/BiVO₄ with 1 wt % CoO_x realizes the best PEC performances (Figure S17).

CONCLUSIONS

In summary, we have constructed stable and efficient NiO/CoO_x/BiVO₄ photoanodes for solar water splitting. The photocurrent densities of the ~6 nm NiO deposited NiO/CoO_x/BiVO₄ photoanode reach 3.5 mA cm⁻² at 1.23 V_{RHE} and 2.5 mA cm⁻² at the small applied potential of 0.6 V_{RHE}, which are 2-fold and 3-fold increase compared to that of the CoO_x/BiVO₄ photoanode. The half-cell solar-to-hydrogen conversion efficiency is up to 1.5% and stoichiometric oxygen and

hydrogen are continuously generated with Faraday efficiency of unity over 12 h. The large PEC improvement is achieved owing to the conformal deposition of the ultrathin *p*-type NiO on the CoO_x/BiVO₄ photoanode for the effective surface states passivation and the enhanced charge separation as evidenced by the enlarged OCP value of ~0.53 V with a fast OCP-decay dynamics indicating the increased mobile photogenerated carriers. Further, the in situ formed NiOOH on the photoanode enables a hydroxyl-rich and hydroxyl-ion permeable surface for the dual catalyst effect of CoO_x and NiOOH to improve the OER activities. The present study demonstrates that the high-efficiency charge separation by ultrathin *p*-type surface modification can effectively improve the PEC performances. This strategy can be applied to other earth-abundant semiconductors with small band gap for wide-energy-range light absorption toward low-cost device for efficient solar fuel generation.

ASSOCIATED CONTENT

Supporting Information

Experimental details of the fabrication of the BiVO₄ photoanodes, electrochemical characterization of the ALD NiO on FTO (Figure S1), ALD NiO growth rate (Figure S2), SEM images of the conformal ALD NiO on the BiVO₄ particles (Figure S3), Mott-Schottky analyses for the ALD NiO layers (Figure S4), chopped-light positive-bias-to-negative-bias LSV scans of the BiVO₄ and the ALD-200-cycle NiO/CoO/BiVO₄ photoanodes (Figure S5), IPCE characterizations (Figure S6), SEM images of the BiVO₄ and the ALD-200-cycle NiO/CoO/BiVO₄ photoanodes before and after PEC measurements (Figure S7), decrease of the photoanodic current with the CoO_x/BiVO₄ photoanodes in LSV scans in new KPi solutions (Figure S8), dark water electrolysis with the CoO_x and NiO/CoO_x electrodes (Figure S9), details of the NiOOH synthesis with XRD characterizations (Figure S10), PEC performances of different BiVO₄ photoanodes in SO₃²⁻ containing solutions (Figure S11), SEM images of the ALD-(100–300)-cycle NiO/CoO_x/BiVO₄ photoanodes after the PEC measurements (Figure S12), electroimpedance spectroscopy of the different BiVO₄ photoanodes (Figure S13), schematic illustrations of the band bending corresponding to the measured absolute OCV_{dark} and OCV_{light} values of different BiVO₄ photoanodes (Figure S14), OCP-decay behavior with the Al₂O₃/CoO_x/BiVO₄ photoanodes (Figure S15), SEM images of the (0–1.5 wt %)-loaded CoO_x/BiVO₄ samples (Figure S16), and PEC performances of the ALD-200-cycle NiO/(0–1.5 wt %)-loaded CoO_x/BiVO₄ photoanodes (Figure S17). This material is available free of charge via the Internet at <http://pubs.acs.org/>.

AUTHOR INFORMATION

Corresponding Author

*domen@chemsys.t.u-tokyo.ac.jp

Notes

The authors declare no competing financial interest.

ACKNOWLEDGMENTS

This work was supported by the Artificial Photosynthesis Project of the Ministry of Economy, Trade and Industry (METI) of Japan, Grant-in-Aids for Specially Promoted Research (no. 23000009) and for Young Scientists (B) (no. 25810112) of the Japan Society for the Promotion of Science (JSPS). A part of work was conducted in Research Hub for

Advanced Nano Characterization, The University of Tokyo, supported by the Ministry of Education, Culture, Sports, Science and Technology (MEXT), Japan. M. Z. thanks Dr. Chaoxia Yuan for the discussions.

■ REFERENCES

- (1) Fujishima, A.; Honda, K. *Nature* **1972**, *238*, 37–38.
- (2) Khaselev, O.; Turner, J. A. *Science* **1998**, *280*, 425–427.
- (3) Grätzel, M. *Nature* **2001**, *414*, 338–344.
- (4) Walter, M. G.; Warren, E. L.; McKone, J. R.; Boettcher, S. W.; Mi, Q.; Santori, E. A.; Lewis, N. S. *Chem. Rev.* **2010**, *110*, 6446–6473.
- (5) Reece, S. Y.; Hamel, J. A.; Sung, K.; Jarvi, T. D.; Esswein, A. J.; Pijpers, J. J. H.; Nocera, D. G. *Science* **2011**, *334*, 645–648.
- (6) Hisatomi, T.; Kubota, J.; Domen. *Chem. Soc. Rev.* **2014**, *43*, 7520–7535.
- (7) Formal, F. L.; Tétreault, N.; Cornuz, M.; Moehl, T.; Grätzel, M.; Sivula, K. *Chem. Sci.* **2011**, *2*, 737–743.
- (8) Du, C.; Yang, X.; Mayer, M. T.; Hoyt, H.; Xie, J.; Mcmahon, G.; Bischofing, G.; Wang, D. *Angew. Chem., Int. Ed.* **2013**, *52*, 12692–12695.
- (9) Kenney, M. J.; Gong, M.; Li, Y.; Wu, J. Z.; Feng, J.; Lanza, M.; Dai, H. *Science* **2013**, *342*, 836–840.
- (10) Li, Y. B.; Zhang, L.; Torres-Pardo, A.; González-Calbet, J. M.; Ma, Y.; Oleynikov, P.; Terasaki, O.; Asahina, S.; Shima, M.; Cha, D.; Zhao, L.; Takanabe, K.; Kubota, J.; Domen, K. *Nat. Commun.* **2013**, *4*, 2566–1–2566–7.
- (11) Minegishi, T.; Nishimura, N.; Kubota, J.; Domen, K. *Chem. Sci.* **2013**, *4*, 1120–1124.
- (12) Kibria, M. G.; Zhao, S.; Chowdhury, F. A.; Wang, Q.; Nguyen, H. P. T.; Trudeau, M. L.; Guo, H.; Mi, Z. *Nat. Commun.* **2014**, *5*, 3825–1–3825–6.
- (13) Hu, S.; shaner, M. R.; Beardslee, J. A.; Licherman, M.; Brunschwig, B. S.; Lewis, N. S. *Science* **2014**, *344*, 1005–1009.
- (14) Boettcher, S. W.; Warren, E. L.; Putnam, M. C.; Santori, E. A.; Turner-Evans, D.; Kelzenberg, M. D.; Walter, M. G.; McKone, J. R.; Brunschwig, B. S.; Atwater, H. A.; Lewis, N. S. *J. Am. Chem. Soc.* **2011**, *133*, 1216–1219.
- (15) Adriana Paracchino, A.; Laporte, V.; Sivula, K.; Grätzel, M.; Thimsen, E. *Nat. Mater.* **2011**, *10*, 456–461.
- (16) Lee, M. H.; Takei, K.; Zhang, J.; Kapadia, R.; Zheng, M.; Chen, Y.; Nah, J.; Matthews, T. S.; Chueh, Y.; Ager, J. W.; Javey, A. *Angew. Chem., Int. Ed.* **2012**, *51*, 10760–10764.
- (17) Jacobsson, T. J.; Fjällström, V.; Sahlberg, M.; Edoffb, M.; Edvinsson, T. *Energy Environ. Sci.* **2013**, *6*, 3676–3683.
- (18) Moriya, M.; Migegishi, T.; Kumagai, H.; Katayama, M.; Kubota, J.; Domen, K. *J. Am. Chem. Soc.* **2013**, *135*, 3733–3735.
- (19) Rao, P. M.; Cai, L.; Liu, C.; Cho, I. S.; Lee, C. H.; Weisse, J. M.; Yang, P.; Zheng, X. *Nano Lett.* **2014**, *14*, 1099–1105.
- (20) Schuh, Y.; Baussart, H.; Delobel, R.; Bras, M. L.; Leroy, J.-M.; Gengembre, L.; Grimblot, J. *J. Chem. Soc., Faraday Trans. 1* **1983**, *79*, 2055–2069.
- (21) Zhang, F.; Yamakata, A.; Maeda, K.; Moriya, Y.; Takata, T.; Kubota, J.; Teshima, K.; Oishi, S.; Domen, K. *J. Am. Chem. Soc.* **2012**, *134*, 8348–8351.
- (22) Tilley, S. D.; Cornuz, M.; Sivula, K.; Grätzel, M. *Angew. Chem., Int. Ed.* **2010**, *49*, 6405–6408.
- (23) Shi, X.; Choi, I. Y.; Zhang, K.; Kwon, J.; Kim, D. Y.; Lee, J. K.; Oh, S. H.; Kim, J. K.; Park, J. H. *Nat. Commun.* **2014**, *5*, 4775–1–4775–8.
- (24) Kim, T. W.; Choi, K.-S. *Science* **2014**, *343*, 990–994.
- (25) Abdi, F. F.; Han, L.; Smets, A. H. M.; Zeman, M.; Dam, B.; Krol, R. V. D. *Nat. Commun.* **2013**, *4*, 2195–1–2195–7.
- (26) Zhong, M.; Ma, Y.; Oleynikov, P.; Domen, K.; Delaunay, J.-J. *Energy Environ. Sci.* **2014**, *7*, 1693–1699.
- (27) Thimsen, E.; Martinson, A. B. F.; Elam, J. W.; Pellin, M. J. *J. Phys. Chem. C* **2012**, *116*, 16830–16840.
- (28) Greiner, M. T.; Helander, M. G.; Tang, W.; Wang, Z.; Qiu, J.; Lu, Z. *Nat. Mater.* **2012**, *11*, 76–81.
- (29) Zhao, Y.; Jermamdez-Pagan, E. A.; Vargas-Barnosa, N. M.; Dysart, J. L.; Mallouk, T. E. *J. Phys. Chem. Lett.* **2011**, *2*, 402–406.
- (30) Zhong, D. K.; Cornuz, M.; Sivula, K.; Grätzel, M.; Gamelin, D. R. *Energy Environ. Sci.* **2011**, *4*, 1759–1764.
- (31) Dong, Y.; He, K.; Yin, L.; Zhang, A. *Nanotechnology* **2007**, *18*, 435602–1–435602–6.
- (32) Trotochaud, L.; Young, S. L.; Ranney, J. K.; Boettcher, S. W. *J. Am. Chem. Soc.* **2014**, *136*, 6744–6753.
- (33) Lin, F.; Boettcher, S. W. *Nat. Mater.* **2013**, *13*, 81–86.
- (34) Gardner, G. P.; Go, Y. B.; Robinson, D. M.; Smith, R. F.; Hadermann, J.; Abakumov, A.; Greenblatt, M.; Dismukes, C. *Angew. Chem., Int. Ed.* **2012**, *51*, 1616–1619.
- (35) Kanan, M. W.; Nocera, D. G. *Science* **2008**, *321*, 1072–1075.
- (36) Barroso, M.; Cowan, A. J.; Pendlebury, S. R.; Grätzel, M.; Klug, D.; Durrant, J. R. *J. Am. Chem. Soc.* **2011**, *133*, 14868–14871.
- (37) Lindahl, E.; Ottosson, M.; Carlsson, J.-O. *Chem. Vap. Deposition* **2009**, *15*, 186–191.
- (38) Miikkulainen, V.; Leskelä, M.; Ritala, M.; Puurunen, R. L. *J. Appl. Phys.* **2013**, *113*, 021301–95.
- (39) Zaban, A.; Greenshtein, M.; Bisquert, J. *ChemPhysChem* **2003**, *4*, 859–864.
- (40) Schlichthörl, G.; Huang, S. Y.; Sprague, J.; Frank, A. J. *J. Phys. Chem. B* **1997**, *101*, 8141–8155.
- (41) Fisher, A. C.; Peter, L. M.; Ponomarev, E. A.; Walker, A. B.; Wijayantha, K. G. U. *J. Phys. Chem. B* **2000**, *104*, 949–958.